Laboratory and numerical investigations on Bénard–Marangoni convection in circular vessels

R. Pasquetti
Lab. J.A. Dieudonné, UMR CNRS 6621, Université de Nice-Sophia Antipolis, Nice, France

P. Cerisier and C. Le Niliot
IUSTI, UMR CNRS 6595, Université de Provence, Marseille, France

This study is concerned with supercritical Bénard–Marangoni flows of a high Prandtl number (Pr≈4000) fluid in cylinders of small to medium aspect ratio, $5 \leq A \leq 10$. Laboratory experiments and numerical simulations, handled with an accurate spectral solver of the unsteady three-dimensional Boussinesq equations, are used to get a good understanding of the flow behavior. Experimental and numerical results are successively presented and then discussed. The confinement effects are especially pointed out and carefully analyzed. © *2002 American Institute of Physics.* [DOI: 10.1063/1.1424307]

I. INTRODUCTION

As is well known since the pioneering works of Pearson[1] and Nield,[2] a horizontal fluid layer heated from below with an upper free surface, may show the so-called Bénard–Marangoni (BM) convection, due to the variations of (i) fluid density (Rayleigh effect) and (ii) surface tension (Marangoni effect) with temperature. Numerous papers have been devoted to the study of such convective flows, using theoretical, numerical, or experimental approaches. We refer to Koschmieder[3] and also to Dijkstra[4] for interesting reviews. In the first theoretical studies on BM convection, the layer was assumed to be infinitely extended in the horizontal direction, i.e., the effect of lateral boundaries was neglected. But experiments necessarily take place in finite vessels where the sidewalls can play an important role on the convective structure. Actually, it can be decisive in small boxes. For instance, experiments performed in small aspect ratio cylinder vessels may show various very different patterns.[5]

This paper is concerned with BM convection in cylinders. Numerical works in such a confined geometry are not so numerous. Among them, Wagner et al.[6] have performed calculations of supercritical BM flows in cylinders of aspect ratio $A \leq 2$, showing the sensitivity to initial disturbances and some possibilities of transition from three-dimensional (3-D) convective patterns to 2-D axisymmetrical ones. Zaman and Narayanan[7] have studied the convective pattern formation, by numerical integration of linearized governing equations. Dauby et al.[8] have conducted a further study in circular vessels, but limited to the weakly nonlinear regime. More recently, using an amplitude equation, Dauby et al.[9] proposed a theoretical analysis of a dynamic mode switching between two two-cell patterns related by a $\pi/2$ rotation about the vertical symmetry axis of the system observed by Johnson and Narayanan[10] in a circular vessel.

Here we are interested in BM supercritical convection in cylinders of small to medium aspect ratio: $5 \leq A \leq 10$, with $A = D/d$ and where D and d are the cylinder diameter and depth, respectively. As already pointed out,[5,7,8] in such geometries the flow may exhibit very different flow structures. At the threshold of the convective motion, this results from the fact that different convective patterns are associated with values of the critical Rayleigh and Marangoni numbers very close to each other.[8] Let us remind ourselves of the expressions of these dimensionless numbers and also of the Biot and Prandtl numbers, respectively, required to model the heat exchange at the upper free surface with the surroundings and to consider the inertial effects:

$$\text{Ra} = \frac{\alpha g \Delta T d^3}{\nu \kappa}, \quad \text{Ma} = -\frac{\partial_T \sigma \Delta T d}{\rho \nu \kappa},$$
$$\text{Bi} = \frac{hd}{\lambda}, \quad \text{Pr} = \frac{\nu}{\kappa}. \tag{1}$$

In these formulas, the usual notations are used: d is the fluid layer thickness, ΔT the vertical temperature gap, ν the kinematic viscosity, κ the thermal diffusivity, α the volume expansion coefficient, g the gravity, ρ the density, $\partial_T \sigma$ (<0) the rate of change of surface tension with temperature, h the mean heat transfer coefficient at the free surface, and λ the thermal conductivity.

Papers on BM cylindrical convection are often devoted to the study of the transition from the conductive to the convective regime, by using stability analyses[8,11] or numerical approaches.[6,7] Here our goal is different, since we are not interested in the determination of the critical values of the Rayleigh and Marangoni numbers, but of the study of supercritical flows. Similarly, the initial flow pattern will not be predicted or observed, e.g., in the celebrated experiments of Ref. 5 but rather induced, especially in the numerical experiments.

Laboratory and numerical experiments are used to carry out the present study. The laboratory experiments, performed in the late 1990's, follow similar ones done previously.[12] However, an infrared (IR) thermography system with real time data processing is used here for the measurement of the
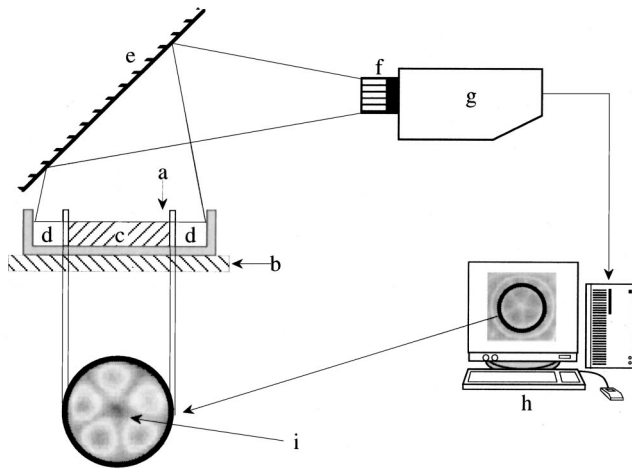
277

FIG. 1. Schematic of the experimental design. (a) Container; (b) heating device; (c) central cells; (d) outer guard ring; (e) 45° inclined aluminum mirror; (f) 7° infrared lens; (g) AGEMA 880 SW — (3–5 μm) infrared scanner; (h) PC frames of 64*128 pixels at 6.25 Hz and 12 bits encoded; the final picture compared with 100 frames; (i) detail of the scanned cells in the container.

superficial temperature field. For the calculations we have used a high accurate spectral Chebyshev–Fourier code, especially developed for the calculation of "Boussinesq flows" in cylinders.[13,14] Preliminary results for BM convection were presented in Ref. 14.

Let us emphasize that we do not plan to produce numerical simulations of particular experiments. This would not be realistic, due to the assumptions used in the modeling: Thus, the heat exchange at the interface oil–air is modeled in a simple way, by using a heat transfer coefficient and a mean temperature of the air, and the variations of the thermophysical parameters with the temperature are not taken into account. Our goal is to investigate the BM convection of a high Prandtl number fluid in cylinders of small to medium aspect ratio with two complementary approaches.

The plan of the paper is the following. In Sec. II we deal with the experimental device and results. The numerical study is presented in Sec. III. In Sec. IV we discuss the results of both approaches and finally offer conclusions in Sec. V.

II. EXPERIMENTS

A. Apparatus

A schematic of the experimental apparatus is shown in Fig. 1. It essentially consists of a cylinder vessel with an inner diameter D (7.4 or 11.2 cm) filled with a silicone oil Rhodorsil 47V500 whose characteristics, at 25 °C and 45 °C, are summarized in Table I. This cylinder is set in another

TABLE I. Approximate values in SI units of the characteristic parameters of the fluid at 25 °C and 45 °C.

T	ρ	$\nu \times 10^4$	$\alpha \times 10^4$	$\kappa \times 10^7$	λ	$\partial_T \sigma \times 10^5$	Pr
25	970	5.0	9.45	1.13	0.16	5.8	4425
45	952	4.0	10.44	1.15	0.16	5.8	3478

vessel that contains the same oil acting as a guard ring. The bottom is flat, horizontal, and made of copper. It is heated by a regulated electric device. The layer depth, d, is measured by using two micrometric comparators (precision ±0.02 mm). The free surface of the liquid is horizontal and in contact with the atmosphere, without a lid. This is the configuration in which we are interested and, moreover, this allows precise measurements of the surface temperature with the thermovision system. The apparatus is placed in a temperature controlled atmosphere (±0.5 °C) and a double door protects the laboratory room from outer perturbations. Moreover, the regulator device maintains the temperature difference between the heating plane and the air, so that even the above-mentioned temperature fluctuations have a negligible influence on the experiment.

To measure the temperature at the bottom we use a very thin thermocouple (diameter 0.05 mm), which ensures a good thermal contact with the copper plate. For the upper free surface, we take an average temperature owing to the thermovision technique that provides instantaneously both the convective pattern and the whole surface temperature field. Infrared thermography is indeed an efficient and nondisturbing means of investigation.

We used an infrared scanner AGEMA 880 Short-Wave, connected to a real time data acquisition system. The infrared pictures are composed of 64×128 pixels and the maximum acquisition frequency is 25 Hz. However, four consecutive frames are interlaced to obtain a good quality picture, so that for a prescribed physical point a 6.25 Hz acquisition frequency is the maximum one. All the measurements provided by the infrared picture are 12 bits encoded. A calibration, using a blackbody within the temperature range 0 °C–50 °C, permits us to obtain the calibration equation.[16] It is then possible to calculate a "blackbody equivalent temperature," T_{bb}. The maximum error is 0.05 °C in this range and the resolution around 30 °C is about 0.03 °C.

Knowing the emissivity ϵ of the scanned surface and the "radiant environment temperature" T_e, the surface temperature T_s is calculated from the relation

$$\epsilon T_s^4 = T_{bb}^4 - (1-\epsilon) T_e^4. \tag{2}$$

The emissivity of the oil was identified by using the hemisphere method.[16] We found $\epsilon \approx 0.9$. To control T_e, the apparatus is placed in a box and its temperature is measured with a thermocouple connected to a digital multimeter. To keep a vertical position to the IR camera, we use an aluminum mirror with reflective factor equal to 0.97 in the SW wavelength range (3–5 μm) of the IR system.

Note that in this SW range the air is transparent, so that there is nearly no attenuation of the IR fluxes. Moreover, the distance experiment camera is short, so that refraction effects are quite negligible. Visualizing the motion of the air is possible by using the shadowgraph technique. This was done in earlier experiments: A "slow," say 1–10 cm s^{-1}, and chaotic motion of the air can be observed, but in any cases the coupling between the convection phenomena in the air and in the oil seems extremely weak. Thus, if one slightly disturbs the air motion above the experiment, one cannot discern any change in the BM pattern, even with the IR camera. In fact,
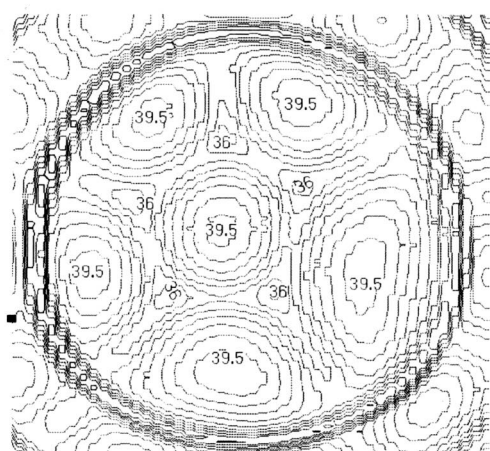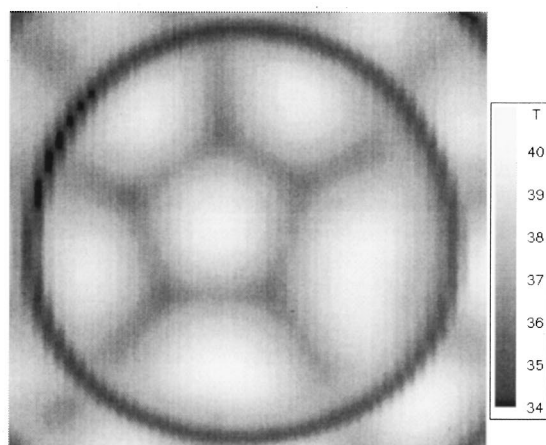
FIG. 2. Surface temperature field from IR thermography.

the time constants, velocities, etc., in the air and in the oil are quite different, so that the influence of the air on the free surface temperature field is averaged. From our point of view, the laminar convective motion in the liquid is thus not strongly coupled to the air turbulent motion but only sensitive to its mean motion. One may think that this gives a justification for simply using a heat transfer coefficient to model the oil–air heat transfer. Also, in the limit of a very thin layer, such that the Rayleigh number of the air convection is below its critical value, then the phenomena are basically different, since the heat transfer in the air is then purely conductive.

To improve the measurement accuracy, the data acquisition system is able to average pictures during the recording procedure. In all experiments we performed averages using 100 frames, so that the measurements are averaged during about 16 s. This time is negligible, even in the transient regime, considering that the evolutions of the phenomena are slow. Figure 2 shows an example of a surface temperature field measurement. Note that on this picture the cells appear to be not exactly of the same size. We attribute this slight loss of symmetry to a small defect of the apparatus levelness, that, however, is estimated better than $\pm 2 \times 10^{-3}$ rd. Con-

cerning the uniformity of the heater temperature field, IR measurements done without oil cannot reveal any nonuniformity.

The liquid movements and the convective pattern can also be made visible by using aluminum powder. We also used this classical technique, in order to obtain clearly visible convective cells (see Fig. 3). In all cases, the two techniques of visualization have shown the same BM patterns. One can only mention that the separation lines between the cells appear generally thicker with the IR camera, which shows a temperature field and not directly the sinking or emerging parts of the convective pattern.

B. Experimental procedure

For each experiment, the liquid is heated during several hours or days to reach a stable state. Then, two procedures can be performed: (i) either a convective structure is imposed according to the thermal technique described in Ref. 12 (generally, it is a hexagon in the center surrounded by six cells); or (ii) the oil is stirred with a rod. The evolution of the pattern is then observed for a day at least (some experiments lasted 38 days). Note that with $d=1$ cm, the viscous and a thermal diffusive characteristic times associated to this length scale are, respectively, $t_\nu = d^2/\nu \approx 0.25$ s and $t_\kappa = d^2/\kappa \approx 0.25$ h. Of course, if D is used as a length scale, these values should be increased by a factor A^2. For experiments corresponding to procedure (i), the central hexagon first relaxes to an optimal size (see Ref. 12) that can be stable or last several hours before rearranging progressively to the final state. For the procedure (ii) a disordered structure first appears, then, after many modifications it reaches the final pattern. In this study, we are only interested in the final pattern.

C. Results

When both procedures (i) and (ii) are performed, the same final pattern is observed. When saying the ''same'' final pattern we mean similar structures but not identical ones: for instance, a pentagon surrounded by five cells in contact with the walls, but the orientation of the structure is different from one experiment to another an two ''same'' structures cannot be strictly superposed.

We performed 19 series of experiments. The characteristics of the experiments, i.e., the aspect ratio, A, the depth layer, d, the Rayleigh number, Ra, the Marangoni number, Ma, and the final structure, FS, are gathered in Table II. Note that in the present experiments the presence of a small meniscus along the vessel walls has no influence on the Bénard–Marangoni (BM) patterns, due to the large sizes of the convective cells.

For the smallest values of A ($A \leqslant 6.21$) the vessel is already sufficiently large to promote the existence of four slice-type cells, with $\pi/2$ periodicity [Fig. 3(a)]. In each cell the fluid rises at the center of the cell and sinks along the rims. The pattern is approximately centered at the vessel axis. If the container is slightly inclined (slope equal to 5 $\times 10^{-3}$), the number of cells is kept but the pattern becomes π periodic. For larger values of A ($6.92 \leqslant A \leqslant 7.72$) a central
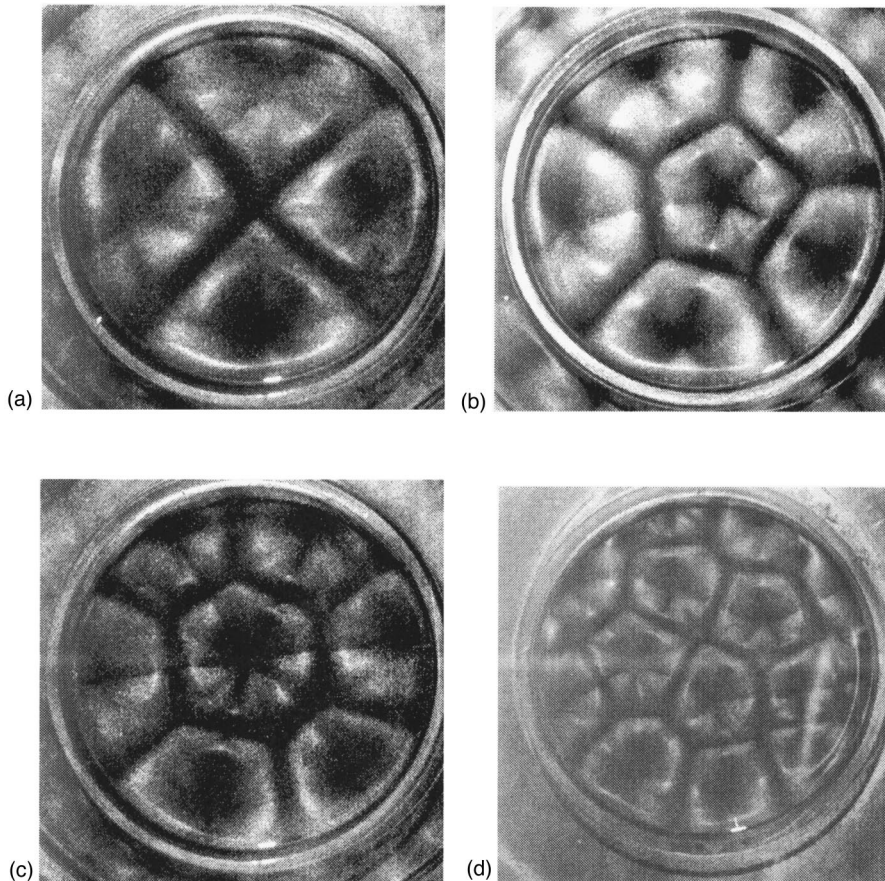
FIG. 3. Flow visualizations with aluminum powder: (a) the four slice-type; (b) the 1–5; (c) the 1–6; and the (d) 4–9 BM patterns.

cell can exist. It is the 1–5 BM pattern, i.e., a pentagon surrounded by five cells [Fig. 3(b)]. For the larger aspect ratio $A=8.1$, one obtains the 1–6 BM pattern [Fig. 3(c)]. Finally, for the greatest value $A=10.47$, the flow structure becomes more complex, since the central cell is now replaced by four pentagonal cells [Fig. 3(d)], surrounded by a set of polygonal cells. Moreover, this structure is always changing, showing alternatively both the 4–8 and 4–9 BM patterns.

TABLE II. Series of experiments with characteristics and the final convective pattern. A: aspect ratio — d; depth layer (mm) Ra: Rayleigh number — Ma: Marangoni number — FS: final structure (the first number shows the number of cells at the vessel center and the second number shows the number of cells along the vessel wall).

Series	A	d	Ra	Ma	FS
1	5.21	14.20	2500	80.4	4
2	5.56	13.30	2030	74.5	4
3	6.17	12.00	1462	65.9	4
4	6.21	11.91	1537	70.6	4
5	6.21	11.91	1626	74.7	4
6-12	6.92	10.70	954	53.9	1-5
13,14	6.92	10.70	1032	58.4	1-5
15	6.95	10.65	1090	62.7	1-5
16	7.08	10.45	900	53.3	1-5
17	7.72	9.58	737	52.3	1-5
18	8.10	9.14	1560	124	1-6
19	10.47	10.70	999	56.6	4-8/9

One can note that the present results follow similar changes when A is increased, as in the results of Koschmieder and Prahl.[5] Moreover, the same single cell BM flow was obtained for the smaller aspect ratio $A=3.63$. Also, for the larger value $A\approx14$, the BM flow shows three concentric rolls of cells. However, in the present study fluid depths are such that 9.14 mm$\leq d\leq$14.20 mm, so that the buoyancy effect is predominant compared to the surface tension effect. To see that readily, one can consider the case of an infinite layer. If Ra_c and Ma_c are the critical values of the Rayleigh and Marangoni numbers and Ra_{c0} and Ma_{c0} those obtained with $\partial_T\sigma=0$ and $g=0$, respectively, then the ratio $r=(Ra_c/Ra_{c0})/(Ma_c/Ma_{c0})$ gives an idea of the relative importance of the buoyancy and surface tension effects. Here the ratio varies from 1.2 to 5.6. In comparison, for the experiments of Koschmieder and Prahl it is about 0.065 to 0.68, so that in their study the surface tension effect was predominant.

III. NUMERICAL INVESTIGATIONS

The first part of this section is devoted to the modeling and to the numerical technique used to solve the fluid flow equations. Numerical results are then presented. In particular, (a) we recover some classical results about the critical value of the Marangoni number, (b) show how the flow development may be sensitive to the initial conditions (to disturbances at the initial time), (c) analyze the change in the flow

structure resulting from a change in the cylinder aspect ratio, and, finally, (d) focus on the possibility of a pentagonal structure of the central convective cell.

A. Modeling and numerical technique

First we introduce the time-dependent governing equations, with their boundary and initial conditions and then give the main features of the spectral method used to compute BM convective flows in cylinders.

1. Modeling

We assume that the velocity and temperature fields are governed by the incompressible Navier–Stokes equations, coupled, within the Boussinesq approximation, to an advection–diffusing equation for the temperature. Then, in dimensionless form, the so-called "Boussinesq equations" read as

$$\frac{1}{\mathrm{Pr}}D_t\mathbf{V}=-\boldsymbol{\nabla}p+\mathrm{Ra}_0\,T\mathbf{e}_z+\nabla^2\mathbf{V},\quad \text{in } \Omega\times(0,t_F),\quad (3)$$

$$\boldsymbol{\nabla}\cdot\mathbf{V}=0,\quad \text{in } \Omega\times(0,t_F),\tag{4}$$

$$D_tT=\nabla^2T,\quad \text{in } \Omega\times(0,t_F),\tag{5}$$

where $\mathbf{e}_z$ is the unit vertical vector, $t\leq t_F$ the time, $\mathbf{V}$ the velocity, p a pressure term, and T the deviation of the temperature from a particular one, e.g., as done hereafter, the surface temperature at the initial time. These variables have been made dimensionless by using the following characteristic values: d, d^2/κ, κ/d, $\rho\kappa^2/d^2$, and ΔT_0, respectively, where ΔT_0 is the initial temperature difference in the fluid layer. The operator D_t stands for the material derivative, i.e., $D_t=\partial_t+\mathbf{V}\cdot\boldsymbol{\nabla}$. The cylindrical domain is noted Ω, such as in the cylindrical coordinate system $(\rho,\,\theta,\,z)$, $\Omega=]0,\,A/2[\times]0,2\pi[\times]0,1[$. Hereafter we distinguish the Rayleigh and Marangoni numbers, Ra_0 and Ma_0, based on ΔT_0, from the time-dependent numbers Ra and Ma, which make use, at a given time, of the mean temperature of the free surface.

To define the boundary conditions, we split the boundary Γ of Ω into three parts: Γ_0, Γ_+, and Γ_-, for the circular, the upper, and the lower parts of the cylinder, respectively.

Then, we assume the following at the rigid walls:

$$\mathbf{V}=0,\quad T=1,\quad \text{on } \Gamma_-,\tag{6}$$

$$\mathbf{V}=0,\quad \partial_\rho T=0,\quad \text{on } \Gamma_0.\tag{7}$$

No-slip conditions are thus imposed to the velocity. For the temperature, one uses Dirichlet conditions at Γ_- (the temperature is imposed at the base of the cylinder) and homogeneous Neumann conditions at Γ_0 (adiabaticity).

With $\mathbf{V}=(V_\rho,\,V_\theta,\,V_z)$, at the free surface we assume

$$\partial_zV_\rho+\mathrm{Ma}_0\,\partial_\rho T=0,\tag{8}$$

$$\partial_zV_\theta+\mathrm{Ma}_0\,\frac{1}{\rho}\partial_\theta T=0,\tag{9}$$

$$V_z=0,\tag{10}$$

$$\partial_zT-\mathrm{Bi}(T_\infty-T)=0.\tag{11}$$

Thus, the free surface and Marangoni effects are modeled in the simplest way, i.e., the deformations of the free surface are not considered and the surface forces are assumed proportional to the horizontal component of the thermal gradient. A Robin condition for the temperature field is assumed: the heat flux density, including both its radiative and convective components, is taken proportional to the temperature difference between the environment temperature T_∞ and the superficial temperature $T(\rho,\,\theta,\,1)$.

For the initial conditions we assume the conductive regime, i.e., the fluid is at rest and the temperature field is linear between the dimensionless temperatures of the bottom wall, $T=1$, and of the free surface, $T=0$. At $t=0$,

$$\mathbf{V}_0=0,\tag{12}$$

$$T_0=1-z.\tag{13}$$

The compatibility of Eqs. (11) and (13) then requires that the scaled environment temperature deviation is given by

$$T_\infty=-\frac{1}{\mathrm{Bi}}.\tag{14}$$

However, since the conductive regime solves the "Boussinesq equations," a disturbance of the temperature field will be used in the numerical experiments to start the convective motion. Moreover, as explained later, this initial disturbance will be used in order to induce specific structures of the flow.

2. Numerical technique

For the sake of completeness we review the main characteristics of the numerical solver, but details on this part can be found in Refs. 13, 14. To enforce the divergence-free feature of the velocity field, one solves the vorticity–vector potential $(\boldsymbol{\omega}-\boldsymbol{\psi})$ formulation of the Navier–Stokes equations. Thus, with

$$\boldsymbol{\omega}=\boldsymbol{\nabla}\times\mathbf{V},\tag{15}$$

$$\mathbf{V}=\boldsymbol{\nabla}\times\boldsymbol{\psi},\tag{16}$$

one obtains

$$\frac{1}{\mathrm{Pr}}\{\partial_t\boldsymbol{\omega}+\boldsymbol{\nabla}\times[\,\boldsymbol{\omega}\times(\boldsymbol{\nabla}\times\boldsymbol{\psi})]\}=\mathrm{Ra}_0(\boldsymbol{\nabla}\times T\mathbf{e}_z)+\nabla^2\boldsymbol{\omega},\tag{17}$$

$$\nabla^2\boldsymbol{\psi}+\boldsymbol{\omega}=0.\tag{18}$$

This set of vectorial equations must be associated with boundary and initial conditions. The initial condition only involves the vorticity and directly results from the one imposed on the velocity:

$$\boldsymbol{\omega}_0=\boldsymbol{\nabla}\times V_0=0.\tag{19}$$

Choosing the boundary conditions is less straightforward (see the earlier works of Refs. 17 and 18). With $\mathbf{n}$ for the outward unit vector normal to Γ, we have used the following set of boundary conditions: everywhere on Γ,

$$\boldsymbol{\nabla}\cdot\boldsymbol{\omega}=0,\tag{20}$$

$$\boldsymbol{\nabla}\cdot\boldsymbol{\psi}=0,\tag{21}$$

$$\psi \times n = 0; \tag{22}$$

at the rigid walls Γ_- and Γ_0:

$$(\nabla \times \psi) \times n = 0; \tag{23}$$

at the free surface Γ_+:

$$\omega_\rho = \text{Ma}_0 \frac{1}{\rho} \partial_\theta T, \tag{24}$$

$$\omega_0 = -\text{Ma}_0 \partial_\rho T. \tag{25}$$

Conditions (20)–(21) make ω and ψ solenoïdal, (21)–(22) ensure the uniqueness of ψ, (23) is the no-slip boundary condition and (24)–(25) result from the definition of the vorticity and from the boundary conditions for the velocity at the free surface.

The partial differential equations (17), (18), (5), associated with the previously mentioned initial and boundary conditions for both the vorticity and temperature fields, are solved as described in Refs. 13, 14. Essentially we have the following.

(i)   Integration in time is performed with a second-order finite difference scheme: Linear terms are treated implicitly (backward Euler approximation) and nonlinear terms explicitly (Adams–Bashforth extrapolation).

(ii)   The approximation in space makes use of a Fourier–Chebyshev pseudospectral method. Thanks to the natural periodicity in θ, the azimuthal direction is handled with Fourier series. Consequently, the 3-D problem splits into a set of 2-D problems, that are solved with a Chebyshev collocation method.

(iii)   Concerning the boundary conditions, at the rigid walls one has five boundary conditions for the vector potential but only one for the vorticity. To recover a more standard situation, with three boundary conditions for each variable, an influence matrix technique is used.

(iv)   No artificial boundary conditions are imposed at the axis of the cylinder: in the ρ direction the Chebyshev–Gauss–Lobatto mesh maps the cylinder diameter and not its radius. Thus, the grid points are only clustered at the real boundary of the computational domain. However, the required regularity properties are enforced at the axis, so that the Laplacian of each scalar or vector field is not singular.

B. Numerical results

Many calculations have been carried out to study the BM flow observed in the laboratory experiments. Neglecting the dependence of the physical parameters on the temperature, these calculations are mainly characterized by the values of the dimensionless Rayleigh and Marangoni numbers at the initial time of calculation, Ra_0 and Ma_0, and by the Biot and Prandtl numbers, Bi and Pr.

For the Prandt number we use Pr=4270. For the pair $(\text{Ra}_0, \text{Ma}_0)$, we essentially present results obtained with (2800, 200) or (2400, 150), such that the final values of the Rayleigh and Marangoni numbers, Ra and Ma, compare to those of the experiments. These values of Ra and Ma take into account the increase of the dimensionless mean superficial temperature $\bar{T}(z=1)$, so that

$$\text{Ra} = [1 - \bar{T}(z=1)]\text{Ra}_0 \quad \text{and}$$
$$\text{Ma} = [1 - \bar{T}(z=1)]\text{Ma}_0. \tag{26}$$

Moreover, knowing that for a particular fluid, with constant thermophysical parameters, $\text{Ra}/\text{Ma} = \text{Ra}_0/\text{Ma}_0 \propto d^2$, one can check that here $d \approx 1$ cm.

Concerning the Biot number, as described in Sec. II the upper surface is open to the laboratory room atmosphere. In such a situation, the heat exchange between the oil and the air can only be approximated through the use of a global heat transfer coefficient and a mean temperature of the air, as, e.g., in Ref. 15. One cannot think indeed to compute the turbulent motion of the ambient air or the radiative exchanges between the experimental device and the room. Of course, the value of such a heat transfer coefficient can only be estimated, without taking into account any time or space variations. We have generally used values yielding results in satisfactory agreement with the experimental measurements, essentially Bi=0.4 and Bi=0.5. Especially, we have tried to preserve the ratio r:

$$r = \frac{[1 - \bar{T}(z=1)]}{(1 - T_\infty)}, \tag{27}$$

of the temperature difference in the fluid layer over the temperature difference between the basis of the cylinder and the ambient temperature. Note that with $d=1$ cm, such values of the Biot number yield a heat transfer coefficient such that $6.4 \leq h \leq 8$ W m^{-2} K^{-1}, which may be considered as a reasonable estimate to represent both the radiative and convective components of the heat flux density. Finally, let us mention that qualitatively we have not observed a high influence of the Biot number value, i.e., the BM pattern has not appeared very sensitive to this parameter in our numerical experiments.

The calculations are also characterized by the numerical parameters, namely, for the time discretization: the time step Δt, and, for the space approximation: the maximum values of the Fourier mode, K, and of the degrees of the polynomial approximation, I and J, in the ρ and z directions, respectively. The corresponding mesh is then $(I+1) \times K \times (J+1)$. If the mesh is too coarse, the numerical results may strongly depend on the space discretization, e.g., yielding a 3-D flow rather than an axisymmetric one, as mentioned in Ref. 6. This is the reason why fine grids have been used in all the computations.

In order to favor the emergence of a particular azimuthal mode, we use a slight perturbation of the temperature field at the initial time. Such an approach may be compared to the "thermal method" mentioned in Sec. II. It avoids the formation of a disorganized flow, which actually needs a long time (and so a high computational cost) to structure itself more or less arbitrarily in a particular organized flow, which in fact, would be nothing but a particular solution of the Boussinesq equations. Thus, rather than letting the flow evolve under the sole effects of the round-off errors, or under the effects of a
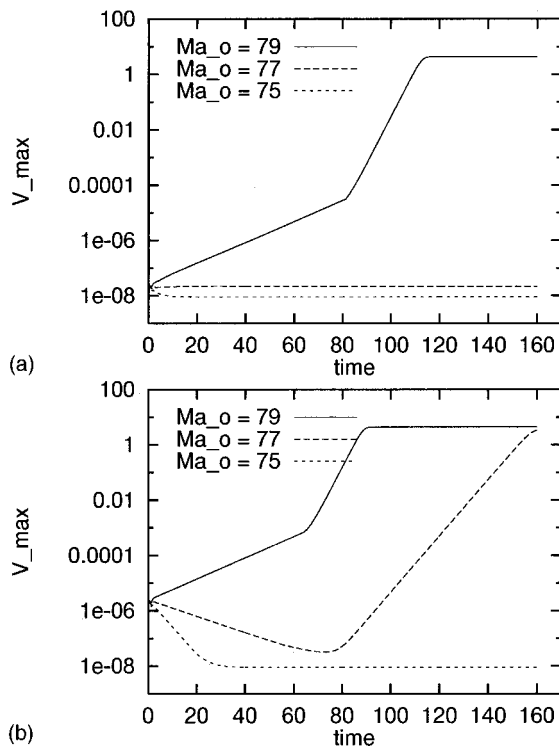
(a)

(b)

FIG. 4. Maximum velocity versus time for $Ma_0 = \{75, 77, 79\}$, with initial disturbances of amplitude (a) 10^{-6} and (b) 10^{-4}.
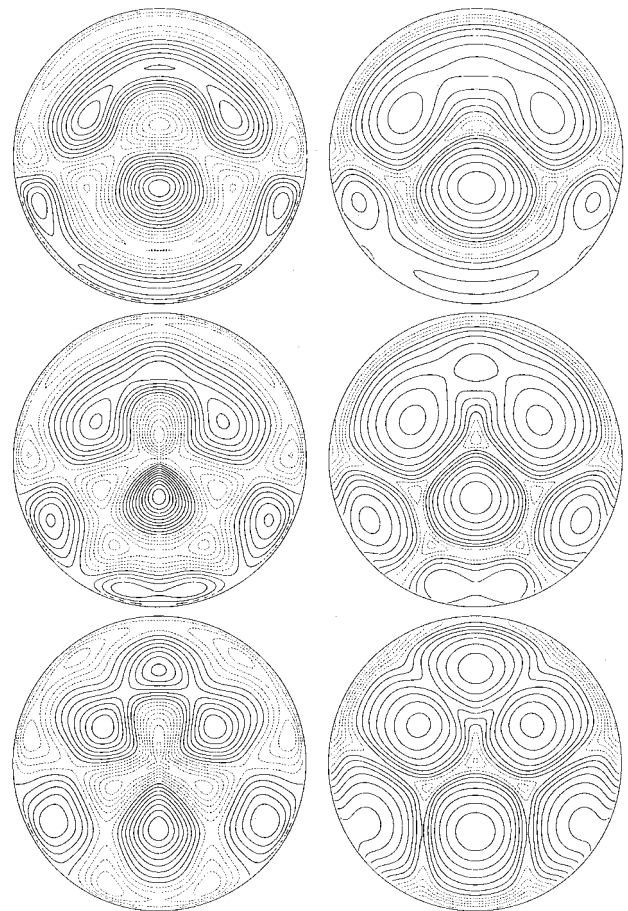

FIG. 5. Isolines of the z component of the velocity at $z=0.5$ and isotherms on the free surface at different times. For $t = \{0.4, 1, 1.6\}$; at left: $V_z(z = 0.5)$; $\delta V_z = 3$, $V_z < 0$ in dashed lines and at the right: $T(z=1)$, $\delta T = 0.05$, $T < 0.2$ in dashed lines ($A = 6.27$, $k_0 = 1$, $Ra_0 = 2800$, $Ma_0 = 200$, $Pr = 4270$, $Bi = 2$).

random perturbation, we prefer to introduce an additive parameter, say k_0, equal to the azimuthal wave number of a sinusoidal perturbation of the initial temperature T_0. Moreover, in a similar way we have often favored an upflow at the axis, essentially to recover the experimental observations. However, this must be done in a slight manner to not induce an axisymmetric flow.

For the values of the dimensionless numbers used in this study, we have always obtained, after the transient part, a steady flow and not, e.g., an oscillatory one, like in Ref. 10 for smaller aspect ratios or, for a larger one, in the series 19 of the present experiments.

1. BM convection at the threshold

First we show that for pure Marangoni convection and with Ma_0, close to the critical value, our numerical results are coherent with the predictions of the stability analyses of Ref. 8.

In Table II of Ref. 8, it is mentioned that for $A=8$ and insulating sidewalls, with $Bi=0.2$, the critical Marangoni number is associated with the azimuthal wave number $k=1$ and equals $Ma_c = 77.87$. Moreover, it is noticed that this value is greater than Nield's value, determined for an infinite layer, which equals 75.544.

Calculations have been performed for three values of the Marangoni number: $Ma_0 = \{75, 77, 79\}$, using a perturbation of amplitude 10^{-6} for the temperature. In Fig. 4, for each value of Ma_0 the evolution of the max norm of the velocity is presented. As expected, one observes that for $Ma_0 = 75$ and $Ma_0 = 77$ the conductive state is going to be recovered, whereas for $Ma_0 = 79$ a convective motion develops. How-

ever, such results depend on the amplitude of the initial disturbance. Thus, when using a perturbation of amplitude 10^{-4}, Fig. 1(b) shows that a convective motion also develops for $Ma_0 = 77$. This points out the transcritical nature of the threshold bifurcation point, as, e.g., mentioned in Ref. 7.

2. Sensitivity to initial conditions

Here we show how the final steady flow pattern may be sensitive to the perturbations of the temperature field at the initial time. To this end, we set the aspect ratio to $A = 6.27$. The Rayleigh and Marangoni numbers equal $Ra_0 = 2800$ and $Ma_0 = 200$ at $t=0$. For the Biot number we use $Bi=2$.

The amplitude of the temperature perturbation at the initial time equals 10^{-3} and we vary the azimuthal wavelength number: $k_0 = 1, \ldots, 6$. For the numerical inputs we use $\Delta t = 10^{-3}$, $I=161$, $J=20$, and $K=90$. The smaller value $I=85$ was first used, but appeared too low to describe the flow pattern evolution computed when starting with $k_0 = 1$ and $k_0 = 3$. The calculations have been carried out until the final time $t_F = 6$.

First we show how a quasisteady flow pattern may be reached, by focusing on the transient flow induced by k_0
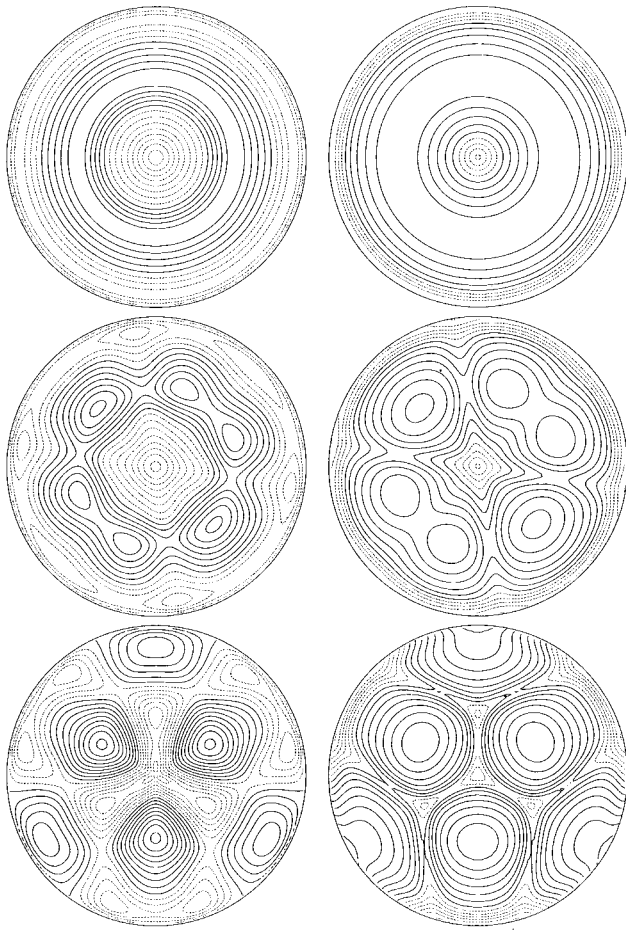
FIG. 6. Isolines of the z component of the velocity at $z=0.5$ and isotherms on the free surface. For $k_0=\{0, 2, 3\}$; at left: $V_z(z=0.5)$; $\delta V_z=3$, $V_z<0$ in dashed lines and at the right: $T(z=1)$, $\delta T=0.05$, $T<0.2$ in dashed lines ($A=6.27$, $t=6$, $Ra_0=2800$, $Ma_0=200$, $Pr=4270$, $Bi=2$).

FIG. 7. Isolines of the z component of the velocity at $z=0.5$ and isotherms on the free surface. For $k_0=\{4, 5, 6\}$; at the left: $V_z(z=0.5)$, $\delta V_z=3$, $V_z<0$ in dashed lines and at the right: $T(z=1)$, $\delta T=0.05$, $T<0.2$ in dashed lines ($A=6.27$, $t=6$, $Ra_0=2800$, $Ma_0=200$, $Pr=4270$, $Bi=2$).

$=1$ and upflow at the axis. Figure 5 presents, at different times $t=\{0.4, 1, 6\}$, the isolines of the z component of the velocity field at mid-depth of the cylinder and the isotherms at the free surface. Stiff changes of the flow structure may be observed, especially because the flow pattern induced by the temperature perturbations and the final one are very different. Thus, the final flow pattern points out a $k=3$ azimuthal wave number, so that $k \neq k_0$, and a downflow rather than an upflow at the cylinder axis.

The different final convective patterns, as the V_z isolines at the mid-depth and the superficial temperature fields, are shown in Figs. 6–7. Essentially, one observes that the azimuthal initial wave numbers:

(i) $k_0=0$ yields a Rayleigh–Bénard (RB) axisymmetric two rolls flow.

(ii) $k_0=3$ yields a $k=3$ BM structure, similar by $2\pi/3$ rotation. This structure is characterized by three main convective cells around the cylinder axis and three secondary cells squeezed along the circular wall.

(iii) $k_0=4$ yields a slice-type $k=4$ structure, similar by $\pi/2$ rotation.

(iv) $k_0=1$ and $k_0=2$ are inducing BM structures similar to those obtained with $k_0=3$ and $k_0=4$, respectively.
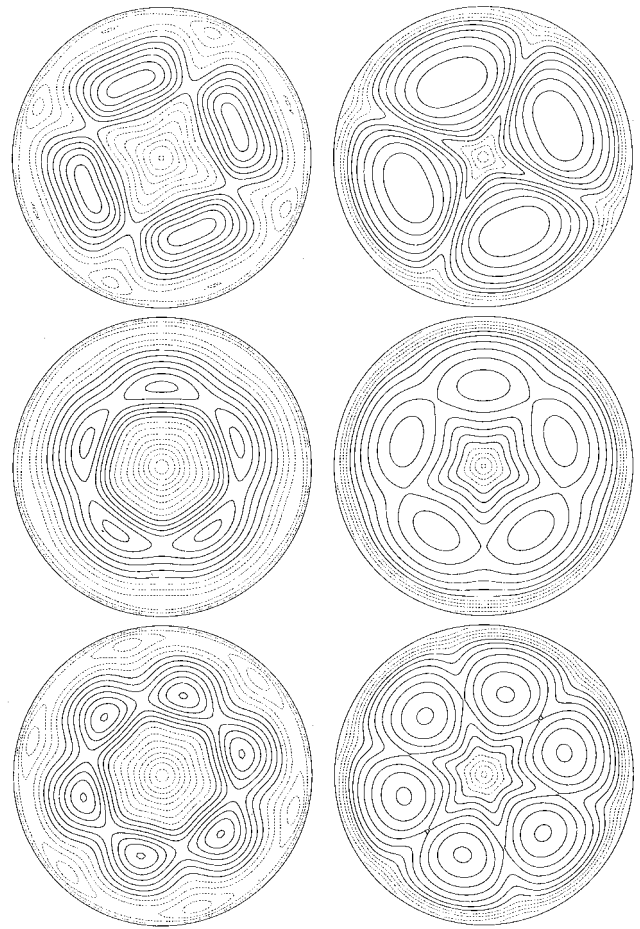
(v) $k_0=5$ and $k_0=6$ lead to mixtures of the $k=0$ two rolls flow and the slice-type $k=5$ and $k=6$ patterns, respectively. However, the $k=5$ structure is worse defined than the $k=6$ and consequently appears very close to the RB axisymmetric flow.

Note that for $k_0=5$ we also tried to vary Ma_0 while keeping constant the ratio Ra_0/Ma_0. The patterns obtained with $Ma_0=120$ and $Ma_0=160$, with $Ra_0/Ma=14$, are similar to the one obtained with $Ma_0=200$.

3. Upflow/downflow at the cylinder axis

For all the flows computed in the previous section a downflow has been obtained at the axis of the cylinder. Focusing on the $k_0=6$ calculation, we want to go from the situation where the fluid sinks at the cylinder axis to the one where it rises.

Such different behaviors may be found for cylinders of aspect ratio $A=7$ and $A=8$, Rayleigh and Marangoni numbers equal to $Ra_0=2400$ and $Ma_0=150$, and a Biot number $Bi=0.4$. At the initial time a $k_0=6$ perturbation of the temperature field is used to induce the $\pi/3$ periodicity. Moreover, an upflow is favored at the axis. For the numerical inputs we use $\Delta t=10^{-3}$, $I=161$, $J=20$, and $K=90$.
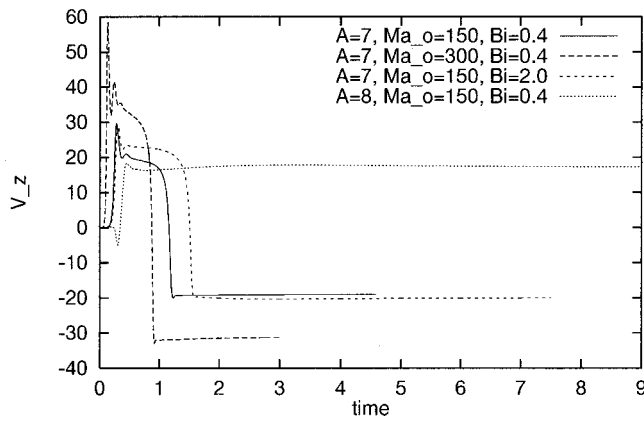
FIG. 8. Vertical velocity at a grid point close to the cylinder axis versus time for $A=7$ and $A=8$ ($k_0=6$, $Ra_0/Ma_0=16$, Pr=4270).

FIG. 10. Vertical velocity at a grid point close to the cylinder axis versus time for $A=\{7, 6, 8, 8.4\}$ ($k_0=5$, $Ra_0=2800$, $Ma_0=200$, Pr=4270, Bi=0.4).

Figure 8 shows the evolution of V_z at a point close to the center of the cylinder, for both cases $A=7$ and $A=8$. One observes, for $t\approx1$, that a stiff sign change occurs for $A=7$, whereas V_z remains positive for $A=8$. Note that computations done with Bi=2 and $Ma_0=300$, $Ra_0/Ma_0=16$, also result in a $k=6$ pattern with downflow at the axis, so that one may think that confinement effects are here really preponderant.

The two "final" flow structures are compared in Fig. 9. Clearly, due to confinement effects for $A=7$ one obtains a $k=6$ slice-type structure, whereas for $A=8$ one obtains the 1–6 BM pattern.

For $A=7$ ($Ma_0=150$, Bi=0.4), at the final time of the computation one gets $\bar{T}(z=1)\approx0.343$, so that $Ra\approx1577$, $Ma\approx98.6$, and $r\approx0.188$. For $A=8$, one obtains $\bar{T}(z=1)$

≈0.356, $Ra\approx1547$, $Ma\approx96.7$, and $r\approx0.184$. Such values of Ra and Ma may be compared to those of series 18, which shows the 1–6 BM pattern.

4. On the 1–5 BM pattern

The experiments described in Sec. II have shown that for intermediate values of the aspect ratio a 1–5 BM flow could be easily obtained. Here we try to recover this BM pattern, since with an aspect ratio $A=6.27$ and an initial wavelength number $k_0=5$ we have obtained a mixture of the $k=0$ two rolls flow and a $k=5$ slice-type structure.

From the conclusions of the previous section, the aspect ratio must be increased. Thus, calculations have been performed for $A=\{7.6, 8, 8.4\}$, for Rayleigh, Marangoni, and Biot numbers equal to $Ra_0=2800$, $Ma_0=200$, and Bi=0.4, respectively. For the calculation parameters we use $\Delta t=2\times10^{-3}$, $I=161$, $J=20$, and $K=90$.

Figure 10 shows, for the three values of A, the evolutions of V_z at a grid point close to the cylinder center. As could be expected, the results are similar to those obtained for the 1–6 BM flow: for the two smallest values of the aspect ratio, one observes a downflow at the cylinder axis, but for $A=8.4$ one gets the desired upflow.

In Fig. 11 are shown the V_z isolines at mid-depth and the isotherms at the free surface for $A=8.4$. The central pentagon
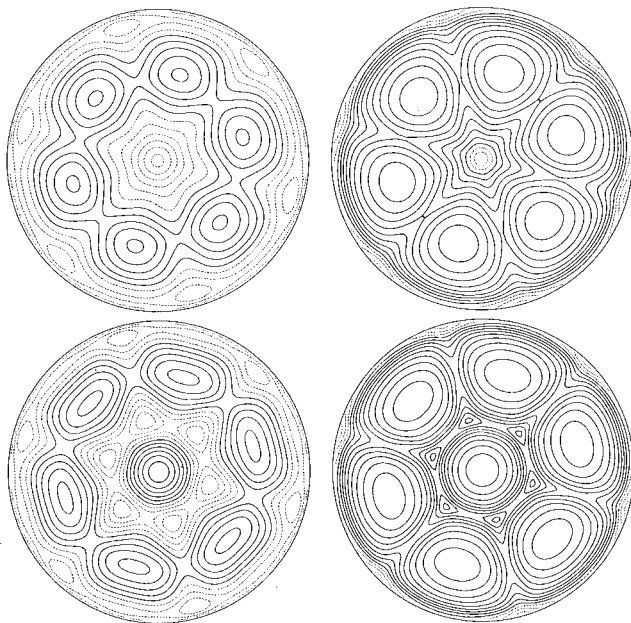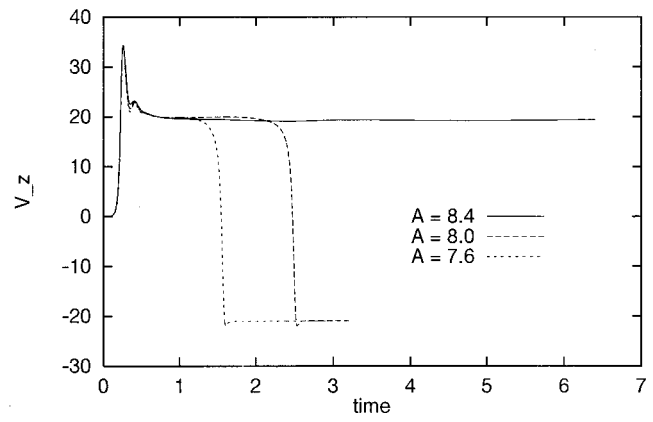

FIG. 9. Isolines of the z component of the velocity at $z=0.5$ and isotherms on the free surface. For $A=7$ and $A=8$; at the left: $V_z(z=0.5)$; $\delta V_z=3$, $V_z<0$ in dashed lines and at the right: $T(z=1)$, $\delta T=0.05$, $T<0.2$ in dashed lines ($k_0=6$, $Ra_0=2400$, $Ma_0=150$, Pr=4270, Bi=0.4).
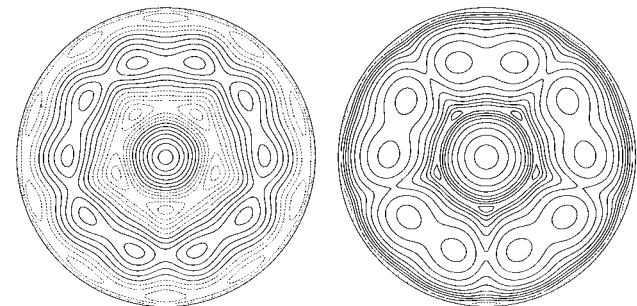

FIG. 11. Isolines of the z component of the velocity at $z=0.5$ and isotherms on the free surface. For $A=8.4$; at the left: $V_z(z=0.5)$, $\delta V_z=3$, $V_z<0$ in dashed lines and at the right: $T(z=1)$, $\delta T=0.05$, $T<0.2$ in dashed lines ($k_0=5$, $Ra_0=2800$, $Ma_0=200$, Pr=4270, Bi=0.4).

can be discerned. However, as previously the 3-D flow structure seems not well defined and now close to a three-roll RB flow.

At the final times of computation we have obtained the following: For $A=7.6$ and $A=8$, $\bar{T}(z=1)\approx0.373$, $\mathrm{Ra}\approx1755$, $\mathrm{Ma}\approx125$, and $r\approx0.179$; For $A=8.4$, $\bar{T}(z=1)\approx0.386$, $\mathrm{Ra}\approx1719$, $\mathrm{Ma}\approx123$, and $r\approx0.175$.

IV. DISCUSSION

This section is devoted to the comparison of the numerical and experimental results. Some features of the computed and observed flows are in satisfactory agreement, whereas for some others discrepancies occur, as discussed now.

For $5.21\leqslant A\leqslant7.72$, the experiments have shown two flow structures, namely the slice-type $k=4$ structure and the 1–5 BM pattern. Moreover, the 1–5 BM pattern has appeared robust, since it was generally obtained without needing to enforce it. For $A=6.27$, the numerical calculations have yielded $k=3$ to 6 slice-type structures, depending on the value of the initial azimuthal wave number k_0, and it has been pointed out that increasing the aspect ratio was needed to obtain the 1–5 and 1–6 BM patterns. Moreover, the 1–5 BM pattern has appeared weakly structured, since the flow computed with $A=8.4$ and $k_0=5$ looks close to an axisymmetric RB flow, with three concentric rolls. More generally, confinement effects due to the lateral wall seem to act differently in the numerical simulations and in the experiments and have appeared more constraining for the former than for the latter. Thus, the 1–5 BM pattern was experimentally observed for $A\geqslant6.92$, whereas a value of $A=8.4$ was required for the calculations.

First, it should be reminded that the characteristic parameters of the flow are not accurately known and, moreover, temperature dependent. Especially, uncertainty on the kinematic viscosity, ν, as given by the manufacturer, may reach 30%. Also, the value of the rate of change of surface tension with temperature, $\partial_T\sigma$, is approximate. Of course, such inaccuracies have a direct influence on the Prandtl, Rayleigh, and Marangoni numbers. Also, one can only have a crude estimate of the Biot number, which depends on the heat-transfer coefficient, which itself results from a modeling of the heat exchanges at the free surface. However, changing the control parameters of the flow was easy to do in the numerical calculations. This has not permitted us to obtain the 1–5 BM pattern in a vessel of small aspect ratio.

Second, an explanation to the fact that the computations have shown more different patterns than the experiments may be found in the transient development of the flow. On the numerical side, a particular structure is induced by enforcing at the initial time an azimuthal wavelength number. In the experiments the "thermal technique" was rarely used, except sometimes to induce the hexagonal pattern. Then, the flow can only form according to the threshold pattern selection and further to the nonlinear interactions. As a result, the numerical procedure used to induce a particular convective structure may yield computed flows never observed in the experiments.

Third, the final time of the computation generally corresponds to a few hours (about 1.5 h with $t_F=6$ and $d=1$ cm). This in, in fact, too short to consider the long time scale dynamics of BM convection. In order to outline this feature, the evolution of the max norm of the temperature time derivative, for the simulations described in Secs. III B 2, III B 3, and III B 4, are plotted in Fig. 10. The first of these graphs clearly shows that the patterns obtained for $k_0=0$, $k_0=3$, and $k_0=6$ are close to the asymptotic ones. Even the exponential-like decay, for $t>4$, allows an estimate of the time constants, say τ, such that $\max|\partial_t T|\propto\exp(-t/\tau)$. We find, for $k_0=0$, $\tau\approx0.414$, for $k_0=3$, $\tau\approx0.666$, and for $k_0=6$, $\tau\approx0.759$. For each of these three values of k_0 the flow seems to behave linearly around the nonlinear asymptotic state, which lends credit to the fact that this asymptotic state is stable. This is less obvious for the other simulations, for which the patterns go on in evolving more strongly. When looking at these patterns (see Figs. 5–7), this is visible for $k_0=1$ and $k_0=2$, since the $\pi/3$ and $\pi/4$ periodicity, respectively, are not yet obtained. For $k_0=4$, one may guess that the $\pi/4$ periodicity will be preserved, in agreement with the experiments. In order to be more confident in this assumption the calculation has been continued: At time $t=12$ the norm of the temperature time derivative goes on in decreasing and equals $\max|\partial_t T|=0.865\times10^{-3}$. A large time constant is obtained for the 1–6 BM pattern with $A=8.4$ (the third graph of Fig. 12): Again one can observe an exponential-like decay, characterized by a time constant $\tau\approx2.094$, which means that the numerical zero is to be obtained for $t\approx50$.

Fourth, using boundary conditions for the temperature in order to isolate the fluid layer from its environment here probably results in an oversimplified modeling. At the free surface, using a mean temperature for the air and a constant heat transfer coefficient supposes that no interactions occur between the turbulent air motion and the convective motion in the liquid. Considering a bilayer oil–air configuration, in Ref. 19 it is pointed out that convection motions in the air and in the liquid may be coupled and that such a coupling has a drastic effect on the critical values of the Rayleigh and Marangoni numbers: the convection in the air sets up transverse temperature gradients at the interface, so that for an air layer thicker than 10 mm the critical Rayleigh and Marangoni numbers are nearly zero. Although the present experiments and the bilayer ones of Ref. 19 are very different, such a phenomenon may explain why the RB axisymmetric flow was never obtained in the experiments, whereas it appears very stable in the calculations. Combined with the confinement effects it may also enforce the well-structured 1–5 BM pattern, when the calculations rather yield a mixture of RB and slice-type flows. Note that this is not in contradiction with the fact that small disturbances of the air motion has no influence on the BM pattern, if one assumes that the convective motion in the fluid layer is only sensitive to the mean motion of the air. Also, assuming adiabaticity at the circular wall of the cylinder is probably crude. Although the radial heat transfer through the sidewall is probably very weak, the circular part of the cylinder behaves like a cooling fin, with a transfer of thermal energy from the heating plate to the ambient air. Moreover, due to the high conductivity of the cyl-
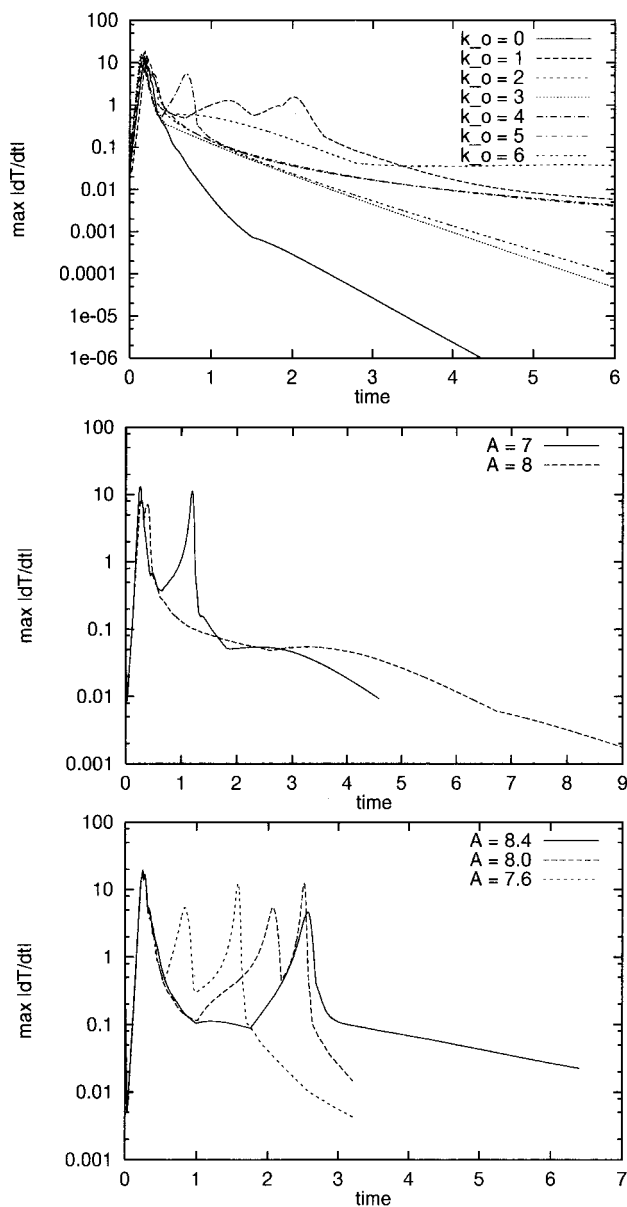
FIG. 12. Max norm of the temperature time derivative versus time for the simulations of Secs. III B 2, III B 3, and III B 4.

inder wall, azimuthal variations of the temperature are immediately damped. This may explain why the $k=3$ slice-type structure, with primary and secondary cells (see Fig. 6), for which maxima and minima of temperature occur at the cylinder wall, was never obtained in the experiments.

Coming back to the first point of the present discussion, changing the control parameters of the flow was easy to do in the numerical calculations. However, this has not permitted us to obtain the 1–5 BM pattern in a vessel of small aspect ratio. In such vessels we have always obtained slice-type convective flows, depending on the k_0 value, like the $k=4$ one, which has also been observed in the experiments. Concerning the second point, one should remark that despite the fact that Rayleigh effects were dominant, the $k=0$ RB axisymmetric flow was never observed in the experiments. On the contrary, such a RB flow is very stable in the calculations. Once the flow has become axisymmetric then the qua-

sisteady state is quickly reached. Concerning the third point, despite the fact that some structures are still evolving, the final BM pattern seems always reached, even if one cannot be sure that some structures may not yet suddenly change. Thus, from our opinion, the last point is decisive. Assuming standard boundary conditions for the temperature yields an oversimplified model, which, on one hand, can yield structures never obtained in the experiments, like the RB axisymmetric flow or the $k=3$ flow with primary and secondary convective cells, but, on the other hand, can only yield, in a vessel of larger aspect ratio, a poorly structured 1–5 BM pattern.

V. CONCLUSION

In this paper we have focused on supercritical BM flows of a high Prandtl number fluid and with predominant buoyancy effects, obtained in cylindrical vessel. Both experimental and numerical approaches have been used to study such flows. Thus, we have given a set of experimental results, meaningful of the numerous experiments that have been performed, and numerical results have been presented, to check the numerical solver, to point out the influence of low-amplitude disturbances of the temperature field at the initial time, to focus on the transition from the $k=6$ BM structure to the 1–6 BM pattern and, finally, to look for the 1–5 BM pattern found in the experiments.

In cylinders of small aspect ratio BM convection exhibits very rich phenomena, so that, as already mentioned, e.g., in Refs. 5, 7, 8, full agreement between theoretical, numerical, and experimental approaches is often difficult to obtain. Here again, a surprising discrepancy has occurred in the intermediate range $6.92 \leq A \leq 7.72$: the 1–5 BM pattern, robust and easy to obtain experimentally was not captured numerically. Instead we have obtained slice-type flows or the RB axisymmetric flow. However, the four slice-type flow observed in the experiments has been computed and, for $A \approx 8$, both experiments and calculations have yielded similar well-structured 1–6 BM patterns.

Our explanation of the discrepancies between experiments and calculations is that using Robin and homogeneous Neumann conditions for the temperature, at the free surface and at the lateral wall of the cylinder, respectively, has led us to an oversimplified modeling. The full modeling of both the fluid layer and its environment being presently out of reach, it would be especially of interest to find our more appropriate boundary conditions to model the heat transfers at the free surface.

ACKNOWLEDGMENT

[1] J. R. A. Pearson, "On convection cells induced by surface tension," J. Fluid Mech. **4**, 489 (1958).

[2] D. A. Nield, "Surface tension and buoyancy effects in cellular convection," J. Fluid Mech. **19**, 341 (1964).

[3] E. L. Koschmieder, *Bénard Cells and Taylor Vortices* (Cambridge University Press, Cambridge, 1993).

[4] H. A. Dijkstra, "Pattern selection in surface tension driven flows," *Free*

Surface Flows, Course, Udine, Italy, 1–5 September 1997, edited by C. H. Hendrik *et al.* (Springer-Verlag, Wien, 1998), CISM, Courses Lect. Vol. 391, p. 101–144.

[5] E. L. Koschmieder and S. A. Prahl, "Surface-tension-driven Bénard convection in small containers," J. Fluid Mech. **215**, 571 (1990).

[6] C. Wagner, R. Friedrich, and R. Narayanan, "Comments on the numerical investigation of Rayleigh and Marangoni convection in a vertical circular cylinder," Phys. Fluids **6**, 1425 (1994).

[7] A. A. Zaman and R. Narayanan, "Interfacial and buoyancy-driven convection—The effect of geometry and comparisons with experiments," J. Colloid Interface Sci. **179**, 151 (2000).

[8] P. C. Dauby, G. Lebon, and E. Bouhy, "Linear Bénard–Marangoni convection in rigid circular containers," Phys. Rev. E **56**, 520 (1997).

[9] P. C. Dauby, P. Colinet, and D. Johnson, "Theoretical analysis of a dynamic thermoconvective pattern in a circular container," Phys. Rev. E **61**, 2663 (2000).

[10] D. Johnson and R. Narayanan, "Experimental observations of dynamic mode switching in interfacial tension convection near a codimension-two point," Phys. Rev. E **54**, R3102 (1996).

[11] S. Rosenblat, S. H. Davis, and G. H. Homsy, "Nonlinear Marangoni convection in bounded layers Part 1—Circular cylindrical containers," J. Fluid Mech. **120**, 91 (1982).

[12] P. Cerisier, C. Pérez-Garcia, C. Jamond, and J. Pantaloni, "A new experimental method to select hexagonal patterns in Bénard–Marangoni convection," Phys. Lett. A **112**, 366 (1985).

[13] R. Pasquetti and R. Bwemba, "A spectral algorithm for the Stokes problem in vorticity-vector potential formulation and cylindrical geometry," Comput. Methods Appl. Mech. Eng. **117**, 71 (1994).

[14] R. Pasquetti, "Vorticity-vector potential formulation of the Navier–Stokes equations: A numerical study," *CFD'94, Conference Proceedings* (Wiley, New York, 1994), pp. 642–649.

[15] J. Pantaloni, R. Bailleux, J. Salan, and M. G. Valarde, "Rayleigh–Bénard–Marangoni instability, new experimental results," J. Non-Equilib. Thermodyn. **4**, 201 (1979).

[16] F. Papini and P. Gallet, *Thermographic Infrarouge* (Masson, France, 1991).

[17] G. J. Hirazaki and J. D. Hellums, "A general formulation of the boundary conditions on the vector potential in three-dimensional hydrodynamics," Q. Appl. Math. **26**, 331 (1968).

[18] S. M. Richardson and A. R. H. Cornish, "Solution of three-dimensional incompressible flow problems," J. Fluid Mech. **82**, 309 (1977).

[19] D. T. Johnson, R. Narayanan, and P. C. Dauby, "The effect of air on the pattern formation in liquid–air bilayer convection—How passive is air?" in *Fluid Dynamics at Interfaces* (Cambridge University Press, Cambridge, 1999).